RSC Advances

PAPER

View Article Online
View Journal | View Issue

Cite this: *RSC Adv.*, 2015, **5**, 17202

Fe(III) induced structural, optical, and dielectric behavior of cetyltrimethyl ammonium bromide stabilized strontium stannate nanoparticles synthesized by a facile wet chemistry route

Astakala Anil Kumar,[a] Ashok Kumar,*[a] J. K. Quamara,[a] G. R. Dillip,[b] Sang Woo Joo[b] and Jitendra Kumar[c]

In this paper, we report the synthesis of Fe containing strontium stannate ($SrSnO_3$) nanoparticles by a facile cost-effective wet chemistry route using cetyltrimethyl ammonium bromide (CTAB) as a surfactant. Thermogravimetric analysis together with differential scanning calorimetric data revealed the formation of $SrSn(OH)_6$ as the initial compound, which led to the formation of $SrSnO_3$ *via* three main endothermic dehydration cycles. The X-ray diffraction patterns of the final compound revealed the formation of the orthorhombic phase of $SrSnO_3$ with *Pbnm* symmetry, and exhibited the contraction of cell volume with increase in Fe content. Raman spectra showed peaks at 220, 256, 306, 404, 452 and 561 cm^{-1}, which corresponds to Sn–O and O–Sn–O band stretching. The band gap values were found to be 4.17, 3.81 and 3.52 eV for the samples with 0, 2 and 4 at% Fe content, respectively. The photoluminescence spectra also confirmed the red shift of band emission peak observed around 370 nm. The relative permittivity was observed to be low and showed steady variation with temperature and Fe content. The dielectric relaxation time was found to decrease with temperature and increase with Fe content. The ac conductivity values were 3.23×10^{-8}, 3.98×10^{-8} and 4.47×10^{-8} Ω^{-1} cm^{-1}, and activation energy was found to be 0.22, 0.34 and 0.44 eV for pristine and Fe (2 and 4 at%). Conductivity analysis suggested the hopping of charge carriers in the crystal, as the possible mechanism for electric conduction.

Received 21st December 2014
Accepted 20th January 2015

DOI: 10.1039/c4ra16775a

www.rsc.org/advances

1. Introduction

Among the perovskite, alkaline earth stannates ($MSnO_3$, M = Mg, Ca, Sr, Ba) form a special class of materials due to their structural, optical, dielectric properties and photovoltaic behavior.[1–4] These properties have been tailored by substituting the host cations by transition metal ions.[5,6] The alkaline earth stannates fall in the class of ferroelectric oxides that are used in the fabrication of electronic components in various electronic devices, such as capacitors, thermistors and transducers, as they have a low temperature coefficient of capacitance.[7] In particular, strontium stannate ($SrSnO_3$) is a wide band gap (~4.1 eV) direct semiconductor and has high resistance at room temperature, in order to enhance the conductivity of these semiconductors it is necessary to dope them with an external atom at the cationic site.[8,9] The perovskite structured strontium stannate nanoparticles are found to possess a steady variation of capacitance with temperature.[10] As technology advances, there is a growing need for electronic components, which operates at a higher frequency and has steady variance of capacitance with temperature at higher frequency to store and transfer a large volume of information. This makes the component fabricated by using these materials to be exploited extensively in telecommunications and radio applications.[11,12] As these materials have potential applications in the fabrication of electronic devices, the synthesis of their low dimensional structures is crucial. The perovskite structured strontium stannate nanoparticles have been synthesized through various techniques such as co-precipitation, solid state reaction, hydrothermal and sol–gel wet chemistry route.[13–16] The sol–gel is one of the promising cost effective techniques to synthesize nanoparticles and gives a considerably high yield of the final product at low decomposition temperatures.[17] Several dopants, such as La, Er, Fe and Co, have been used to engineer the behavior of $SrSnO_3$.[18,19] It was reported that the dielectric and conducting behavior of $SrSnO_3$ has been enhanced by the substitution of the host cations with rare earth metal ions.[20] However, the relaxation behavior of Sr substitution by Fe in $SrSnO_3$ has not been studied yet. Furthermore, as the structural changes in a system affects the physical and optical properties,

[a]*Department of Physics, National Institute of Technology Kurukshetra, Haryana 136119, India. E-mail: ashokku@nitkkr.ac.in; Tel: +91-1744133498*

[b]*School of Mechanical Engineering and Technology, Yeungnam University, Gyeongsan, 712-749, South Korea*

[c]*Materials Science Programme, Indian Institute of Technology Kanpur, 208016, India*

a detail study of the dielectric and allied properties of Fe substituted strontium stannate have greater significance in order to have a complete picture of the dielectric behavior of the wideband gap strontium stannate nanoparticles. There are few reports available on the optical and conductivity behavior of $SrSnO_3$ nanoparticles with different transition metal ion substitution.[21,22] Moreover, the dielectric relaxation of transition metal ion doped $SrSnO_3$ is not yet studied. The present study provides a correlation between the structural, optical and dielectric behavior of the pristine and Fe doped perovskite $SrSnO_3$ nanoparticles synthesized by a facile wet chemistry route, which were stabilized by cetyltrimethyl ammonium bromide (CTAB).

2. Experimental

The Fe substituted strontium stannate nanoparticles with general formula $SrSn_{1-x}Fe_xO_3$ ($0 \leq x \leq 0.04$) have been synthesized by a facile cost-effective wet chemistry route using cetyltrimethyl ammonium bromide (CTAB) as a surfactant. The presence of the surfactant can alter the surface energy of the crystal surfaces and promotes the anisotropic growth of nanoparticles. In the present study, CTAB was used as a surfactant, which plays a major role in the monodispersion of the as synthesized nanoparticles, as is illustrated in Scheme 1. First, the aqueous solution of tin chloride ($SnCl_2 \cdot 2H_2O$) and ferric nitrate $Fe(NO_3)_3 \cdot 9H_2O$ was obtained and subsequently the former solution was added dropwise into the aqueous solution of strontium nitrate ($Sr(NO_3)_2$). Then, CTAB was added to the above solution, maintaining the 0.03 mM concentration in the final solution. The resulting solution was stirred at 80 °C for 4 h to obtain the gel, followed by drying at 100 °C for 2 h and these powders were washed several times with ethanol to remove surface impurities and the polymer present in the compound. These dried powders were calcined at 650 °C for 2 h to obtain the Fe (0, 2, 4%) doped $SrSnO_3$ nanoparticles. The diagram for the synthesis of $SrSnO_3$ nanoparticles is given in Scheme 1. Thermogravimetric analysis (TG) and differential scanning calorimetry (DSC) was performed collectively by using the SDT-Q600 Thermal Analyser. The DSC-TG analysis was performed in nitrogen atmosphere at a heating rate of 5 K min^{-1}. The phase(s) of the synthesized perovskite pristine and Fe (2 and 4 at%) $SrSnO_3$ nanoparticles were analyzed by using a PAN analytical X'pert pro X-ray diffractometer using CuK_α radiation (λ = 1.541874 Å, $K_{\alpha1}/K_{\alpha2}$: 2/1) at 40 kV and 30 mA. The data recorded over a 2θ range of 20–80° with step size as 0.03° min^{-1}. The morphological characterization of the as-synthesized samples was performed by using a transmission electron microscope (Tecnai G2 F20 S-Twin) with an accelerating voltage of 200 kV. Raman spectra were collected using a LABRAM HR 800 micro Raman spectrometer in the range of 150–800 cm^{-1} using a solid state laser with wavelength of 633 nm. The diffuse reflectance spectra of powders in the solid state were recorded by a UV-visible spectrometer, PG instruments Pvt. Ltd T90+ in the spectral range of 230–700 nm. Photoluminescence spectra were collected in the wavelength range of 320–550 nm with an excitation wavelength of 290 nm using a Simadzu RF-530 spectroflurometer. X-ray photoelectron spectra (XPS) were recorded with a Thermo Scientific K-alpha X-ray photoelectron spectrometer having a monochromatic Al-Kα source. The impedance analysis at different temperatures was performed using Aglient E 4980A, Precision LCR Meter in the frequency range between 20 Hz and 2 MHz.

3. Results and discussion

3.1 Structural and phase analysis

Fig. 1(a) shows the variation of the weight (of the powder obtained after drying the gel at 100 °C) in nitrogen atmosphere as the function of temperature in the range of 300–1200 K at a heating rate of 5 K min^{-1}. The three stages of weight loss are clearly visible. The first stage (~300–410 K) was observed to be faster as compared to the second (~410–720 K) and third (~720–840 K) stages. However, the third stage that took place *via* one fast and one slow dehydration steps reveals the fastest water removal rate in its first half cycle. The initial compound obtained after drying the gel was assumed to be $SrSn(OH)_6$, and the intermediate products formed in all the three stages as per weight estimates were assumed as $SrSnO(OH)_4$, and $SrSnO_2(OH)_2$. The weight loss was found to be approximately 6.4%, 6.2% and 6.1% (for all the observed three stages) and matched well with the theoretical estimates. In the first stage, the weight

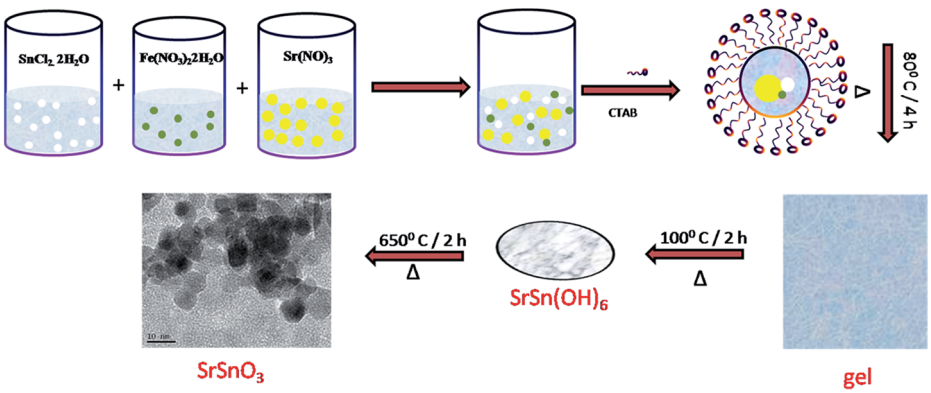

Scheme 1 Showing the synthesis of $SrSnO_3$ nanoparticles.

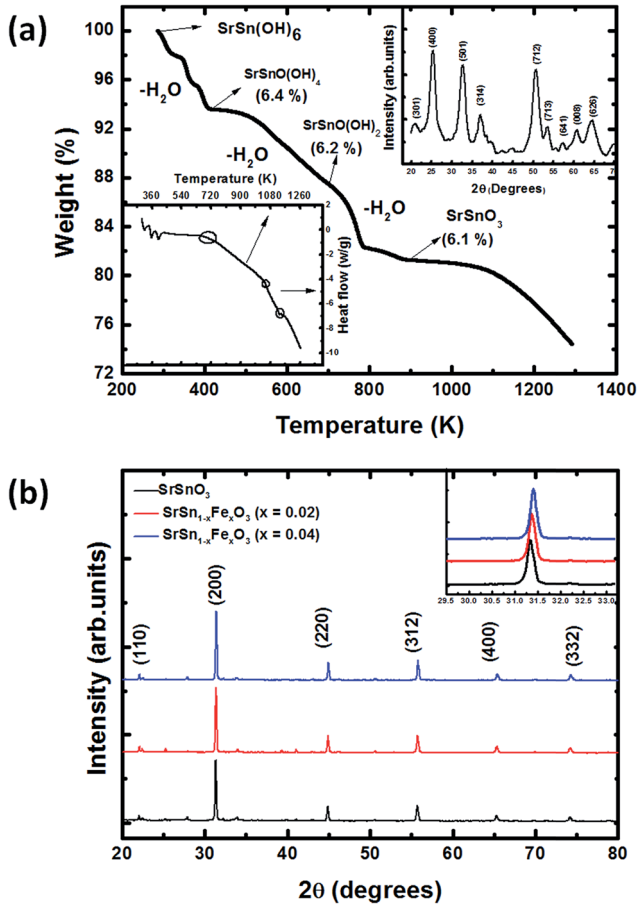

Fig. 1 (a) The thermo gravimetric analysis of the powder obtained by the heating of the gel product at 80 °C for 4 h formed through wet chemistry reaction, and drying subsequently at 100 °C for 2 h; bottom left inset shows the differential thermal analysis of $SrSn(OH)_6$ nanoparticles, top right inset shows the X-ray diffraction pattern of the $SrSn(OH)_6$ nanoparticles, and (b) X-ray diffraction pattern of $SrSnO_3$ nanoparticles with Fe content of 0, 2 and 4 at%; inset shows the details of the peak ($2\theta = 31.33$).

loss was observed to be in three steps with the intermediate products formed to be as $SrSnO(OH)_4 \cdot 2/3H_2O$, $SrSnO(OH)_4 \cdot 1/3H_2O$ and $SrSnO(OH)_4$, corresponding to weight loss of 2.2, 2.1, and 2.1%, respectively. The second stage revealed a weight loss of 6.2%, which corresponds to the loss of one water molecule, and the third stage showed a weight loss of 6.1%, which approximately corresponds to the loss of one water molecule yielding $SrSnO_3$. The bottom left inset of Fig. 1(a) shows the differential scanning calorimetry (DSC) of the dried gel product (confirmed as $SrSn(OH)_6$ by thermogravimetry analysis). The phase changes observed in DSC were in accordance with the weight loss steps observed in thermogravimetric analysis (TGA). There was no weight loss corresponding to CTAB as it was removed through multiple rinsing cycles with ethanol and has been shown in Section 3.2. The top right inset of Fig. 1(a) shows the X-ray diffraction (XRD) pattern of the abovementioned powder obtained by the heating of the gel product (formed through wet chemistry reaction) at 80 °C for 4 h. It reveals diffraction peaks at 2θ values of 20.06, 25.43, 32.83, 36.97, 50.76, 53.65, 56.90, 60.37 and 65.56° corresponding to Bragg reflection planes (301), (400), (501), (314), (712), (713), (641), (008) and (626), respectively, of the strontium tin hydroxide ($SrSn(OH)_6$) with hexagonal type-structure. The lattice constant values were found to be 'a' = 16.18 and 'c' = 12.19 Å, and are in good agreement with the standard data (JCPDS #09-0086).

The X-ray diffraction patterns of Fe (0, 2 and 4 at%) doped $SrSnO_3$ nanoparticles are shown in Fig. 1(b). The diffraction peaks of pristine $SrSnO_3$ were observed at 2θ values of 22.1°, 31.33°, 44.8°, 55.7°, 65.3° and 74.2° corresponding to the Bragg planes (110), (200), (220), (312), (400) and (332), respectively. The planes indexed according JCPDS no. 77-1798, which indicates the formation of highly crystalline orthorhombic phase of $SrSnO_3$. The lattice constant values of pristine $SrSnO_3$ were calculated as $a = 5.7$ Å, $b = 5.7$ Å and $c = 8.09$ Å. A slight shift in the diffraction peaks towards higher 2θ values was observed with the incorporation of Fe^{3+} in the host lattice at the Sn^{4+} site. The ionic radius of Fe^{3+} (0.64) was slightly smaller than the ionic radius of Sn^{4+} (0.69); therefore, the substitution of Fe^{3+} at the Sn^{4+} site resulted in the lattice contraction.

The surface morphology of synthesized perovskite structured strontium stannate nanoparticles have been studied by using high resolution transmission electron microscopy (HRTEM). The TEM images of pristine and Fe (4%) doped strontium stannate nanoparticles are shown in Fig. 2(a)I and (b)I, respectively. The TEM images clearly show the formation of nanoparticles with particle size of about 20 nm. The HRTEM images of pristine and Fe (4%) doped strontium stannate nanoparticles are shown in Fig. 2(a)II and (b)II respectively. The measured d-spacing was about 0.288 nm, which corresponds to the (200) reflection of the orthorhombic phase. The inset of Fig. 2(a)II and (b)II shows the selected area electron diffraction patterns of the single crystal and the reflections are indexed, which are in accordance with X-ray diffraction results shown in Fig. 1(b). The elemental mapping of Sr, Sn and O, which were the constituent elements in strontium stannate nanoparticles are shown in Fig. 2(a)III–V, respectively and Fig. 2(b)III–VI shows the elemental mapping of Sr, Sn, Fe and O of Fe (4%) doped strontium stannate nanoparticles. The corresponding EDS spectra of pristine and Fe (4%) doped strontium stannate nanoparticles are shown in Fig. 2(a)VI and (b)VII, which clearly shows that the final compound was composed of constituent elements, such as Sr, Sn, O and Fe respective of their composition and no other impurity was detected. The atomic composition and chemical nature of the surface of pristine and Fe (2 and 4 at%) doped $SrSnO_3$ nanoparticles were investigated by using X-ray photoelectron spectroscopy (XPS). Fig. 3(a–d) shows the high resolution XPS spectra of Sn 3d, Sr 3d, O 1s and Fe 2p, respectively. Fig. 3(a) shows the high resolution spectra of O 1s for pristine and Fe (2 and 4 at%) doped $SrSnO_3$ nanoparticles, which consist of two peaks at 531.8 and 533.3 eV. The first one corresponds to the O 1s, which was assigned to the $SrSnO_3$ host lattice and second peak at 533.3 eV corresponds to the hydrated oxide species in the samples. Fig. 3(b) shows the Sn 3d photoelectron peak for pristine and Fe (2 and 4 at%) doped $SrSnO_3$ nanoparticles. The Sn 3d was splitted into a doublet. The two peaks observed at 484.8 and 493.2 eV

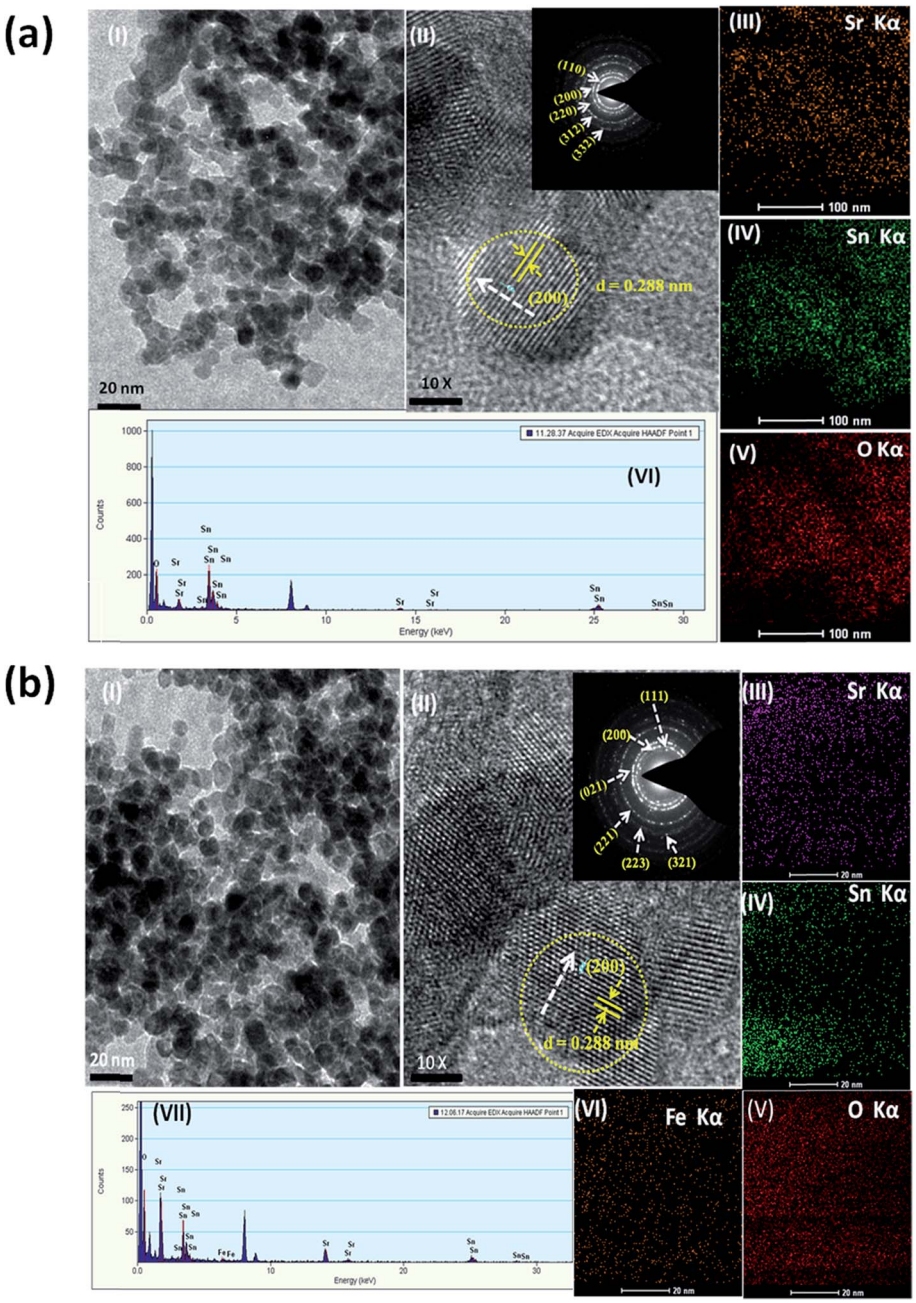

Fig. 2 (a) (I) HRTEM image, (II) lattice fringe pattern, inset shows the SAED pattern, (III–V) elemental mapping of Sr, Sn and O, and (VI) EDS spectra of pristine $SrSnO_3$ nanoparticles. (b) (I) HRTEM image, (II) lattice fringe pattern, inset shows the SAED pattern, (III–VI) elemental mapping of Sr, Sn, O and Fe and (VII) EDS spectra of Fe (3 at%) doped $SrSnO_3$ nanoparticles.

correspond to the Sn $3d_{5/2}$ and Sn $3d_{3/2}$, respectively, have an energy separation of 8.37 eV, which was similar to that of Sn 3d (8.5) in SnO_2,[23] confirming the chemical state of Sn at the surface as +4. The FWHM values were observed to decrease with the increase in Fe^{3+} concentration, which depicts the incorporation of Fe in the lattice at the desired Sn site. Fig. 3(c) shows the high resolution XPS spectra of Sr 3d photoelectron peak for pristine and Fe (2 and 4 at%) doped $SrSnO_3$ nanoparticles, which was splitted into two peaks with binding energy 135.5 and 133.8 eV corresponding to Sr $3d_3$ and Sr $3d_5$, respectively. Fig. 3(d) shows the high resolution XPS spectra of Fe (2 and 4 at%) doped $SrSnO_3$ nanoparticles. The Fe 2p peak was observed at 710.6 eV, which was assigned to Fe $2p_{1/2}$ with Fe showing +3 oxidation state.

3.2 Optical characterization

Fig. 4(a) shows the Raman spectra of pristine and Fe^{3+} (2 and 4 at%) doped $SrSnO_3$ nanoparticles. X-ray diffraction studies in Section 3.1 indicated that there was no change in the orthorhombic structure with the incorporation of Fe^{3+} in the lattice.

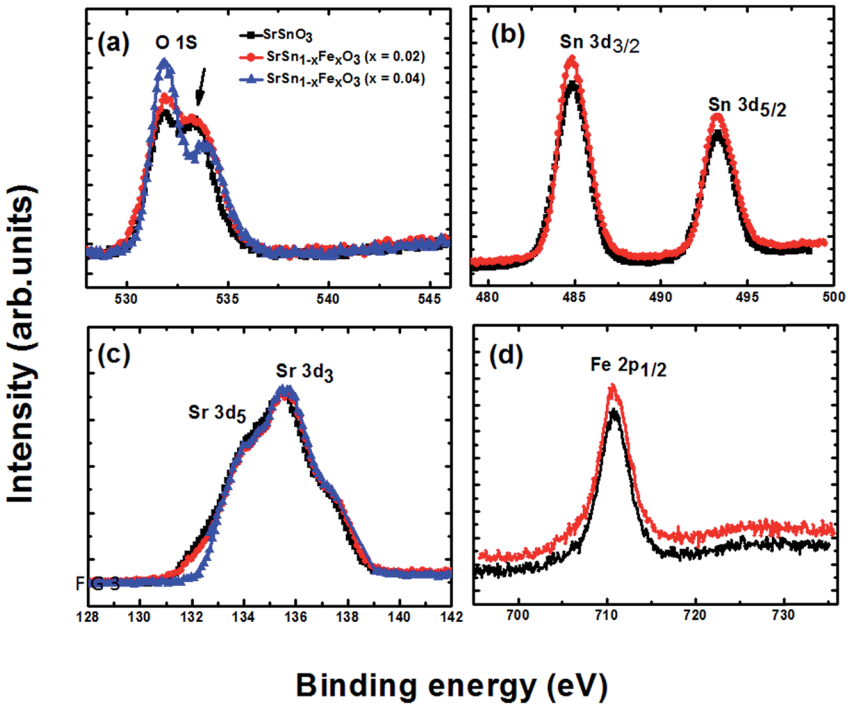

Fig. 3 (a–d) High resolution X-ray photoelectron spectroscopy spectra of Sr 3d, Sn 3d, O 1s and Fe 2p orbitals.

The $SrSnO_3$ was of orthorhombic structure with the point group D_{2h} and space group *Pbnm* (D_{162h}).[23] The Raman active modes for the *Pbnm* space symmetry were $\Gamma_{Raman} = 7A_g + 5B_{1g} + 7B_{2g} + 5B_{3g}$.[24] In the Raman spectra of the pristine and Fe^{3+} (2 and 4 at%) doped $SrSnO_3$ perovskite, the bands at 166, 220, 256, 306, 404, 452, 561, 640, 706 cm^{-1} were observed. The sharp peak observed around 220 cm^{-1} was attributed to A_g mode corresponding to Sn–O–Sn bond and the peak at 256 cm^{-1} was associated with O–Sn–O bond.[25] The peak observed around 306 cm^{-1} was due to the B_{2g} mode corresponding to O–Sn–O bond. The bands at 306 and 404 cm^{-1} were related to the SnO_3 torsional mode and the peak at 561 cm^{-1} was related to the Sn–O stretching. The Raman peaks of corresponding wave number were red shifted with the increase in the Fe^{3+} content in the lattice, which was possibly the result of the increase in the particle size and effective bond length change due to reduced Coulomb force by Fe^{3+} in comparison to Sn^{4+}. The inset of Fig. 4(a) shows the Fourier transform infrared (FTIR) spectra of pristine and Fe (2 and 4%) doped $SrSnO_3$ nanoparticles. The peak observed around 3452 cm^{-1} and 1634 cm^{-1} represents the O–H stretching and O–H bending vibration of water molecules, respectively, adsorbed on the surface of as-synthesised nanoparticles.[26] The peaks observed around 651 and 544 cm^{-1} correspond to the O–Sn–O bridging and Sn–OH terminal bonds, respectively.[27] The peak centered around 1496 cm^{-1} corresponds to the asymmetric stretching vibration of Sn–OH bonds[28] and the peak observed around 930 cm^{-1} was attributed to the vibration of carbonyl groups.[29] Furthermore, Gökce *et al.*[30] theoretically calculated the vibration frequencies of the CTAB molecule using *ab initio* Hartree–Fock and density functional theory, and compared with experimental findings. In the present study, the FTIR absorption spectra (inset Fig. 4(a)) together with Raman Spectra (Fig. 4(b)) do not exhibit any signature of CTAB presence.

The top left corner inset (I) of Fig. 4(b) shows the absorption spectra of pristine and Fe^{3+} doped $SrSnO_3$ nanoparticles. These show the strong absorption in the UV region. The optical absorption edge in pristine $SrSnO_3$ was observed around 290 nm, and found redshifted with increase in the doping concentration. The band gap values of the as-synthesized samples were estimated from diffuse reflectance spectra by plotting the square of multiple of Kubelka–Munk ($F(R)$) function with the square of energy ($h\nu$) *versus* $h\nu$, which is shown in the Fig. 4(b). The extrapolated linear part of the curve at $F(R)^2 = 0$ gives the band gap of the as synthesized samples (Fig. 4(b)I). The band gap values of $SrSnO_3$ nanoparticles are found to be 4.17, 3.81 and 3.51 eV for the Fe content of 0, 2 and 4%, respectively. The incorporation of Fe^{3+} in the host lattice resulted in the increase in the particle size; therefore, a decrease trend in the band gap was observed. Moreover, in $SrSnO_3$, the Sn^{4+} ions are in octahedral symmetry and $3d^5$ spin states of Fe^{3+} splits into two degenerate e_g and three degenerate t_{2g} orbitals. Thus, the incorporation of Fe^{3+} in the lattice results in the formation of intermittent energy states in the band gap region of $SrSnO_3$, which in turn results in the reduction of band gap. The bottom right corner inset (II) of Fig. 4(b) shows the room temperature photoluminescence spectra of pristine and Fe^{3+} doped (2 and 4 at%) $SrSnO_3$ nanoparticles recorded at an excitation wavelength of 290 nm. Two intense peaks were observed at wavelength of 360 and 470 nm for pristine $SrSnO_3$ and a redshift was observed for the Fe (2 and 4 at%) doped samples. The band gap energy of these peaks observed at 360 nm

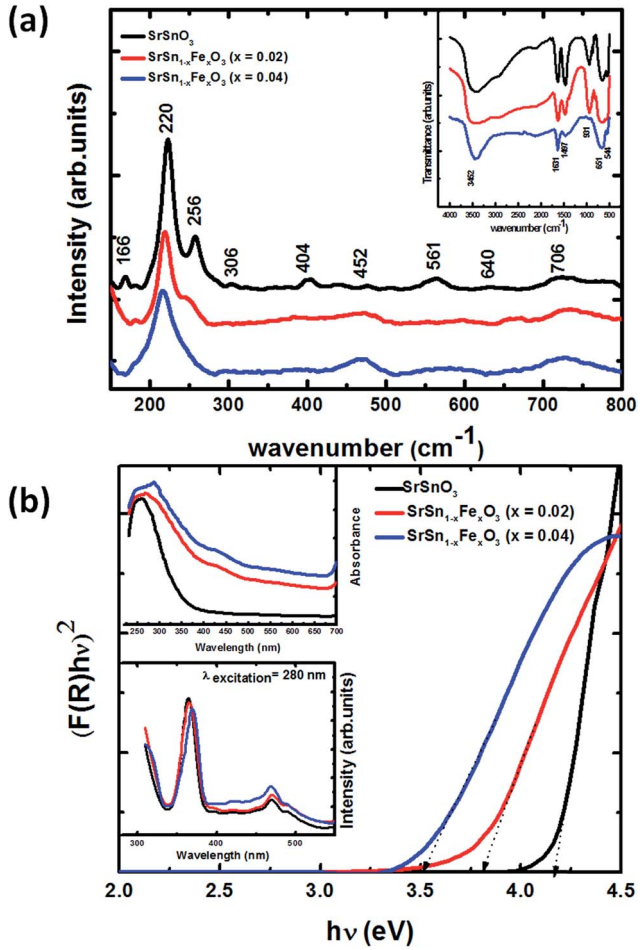

Fig. 4 (a) Raman spectra of pristine and Fe doped $SrSnO_3$ nanoparticles; inset shows the Fourier transform infra-red spectra of pristine and Fe doped $SrSnO_3$ nanoparticles (b) Tauc's plots for band gap estimation for pristine and Fe doped $SrSnO_3$ nanoparticles; top left corner inset (I) shows the absorption spectra, and the bottom left corner inset (II) shows the photoluminescence spectra for the pristine and Fe doped $SrSnO_3$ nanoparticles.

corresponds to the band gap values calculated from the absorption spectrum corresponding to the direct allowed transition between O 2p and Sn 5s energy levels.[31] The Sn^{4+} has higher charge than Fe^{3+} ions and as a result of charge balance there will be an increase in the oxygen vacancies in the host lattice, due to which the reduction in the intensity of PL peaks observed. The other peak observed at 470 nm corresponds to the emission occurred from the various defect energy levels, which were in the band gap region. The population of these defect levels was found to increase with increase in Fe content.

3.3 Dielectric properties

The variation of relative permittivity (ε') as a function of frequency at various temperatures for pristine and Fe (2 and 4 at%) containing $SrSnO_3$ samples obtained by the pelletization of respective nanopowders and subsequent sintering at 923 K for 2 h are depicted in Fig. 5(a–c). Two distinguishable regions were clearly observed: (i) the plateau region at higher frequency and (ii) the dispersive nature at the lower frequency. The ε' decreases with increase in frequency, which was due to the fact that at lower frequency ε' varies with deformational and relaxation polarization mechanisms. The deformational polarization mechanism depends on the displacement of charge carriers, whereas relaxation mechanism depends on the orientation of charge carriers in the influence of an external electric field; however, at a higher frequency there will be a decrease in the orientation polarization, as the molecular dipoles take more time to change their orientation under the influence of external electric field. The ε' was found to increase with increase in the ferric ion content. From Section 3.2 it was observed that the band gap decreases with increase in the doping concentration. The dielectric constant increases with decrease in the band gap, this can be explained by using the electronic polarizability phenomenon. If the band gap decreases further, the electron in the valence band tend to move to the conduction band more easily and the energy gap between the bonding and antibonding states decreases, as a result, the corresponding wave function can be easily altered by varying the external electric field. Therefore, the dielectric constant increases as the electron polarizability increases.[32] The insets of Fig. 5(a–c) show the variation of dielectric loss tangent ($\tan\delta$) as a function of frequency at various temperatures. The peaks were observed in the plot of loss tangent as a function of frequency, which indicates the presence of relaxation mechanism. The relaxation peaks were shifted towards the higher frequency, indicating that the charge carriers inside the sample were thermally activated. The relaxation time was found to decrease with temperature and tend to increase with increase in ferric ion concentration as the charge carriers increases, and it was difficult for the diploes to align into the initial position, which tend to enhance the relaxation time. The variation of relaxation time with temperature and Fe content is shown in Fig. 5(d).

3.4 Temperature and frequency dependence on ac conductivity

Fig. 6(a–c) show the variation of ac conductivity as a function of frequency at different temperatures. The ac conductivity as a function of frequency $\sigma(\omega)$ is given by the relation, $\sigma(\omega) = \omega\varepsilon_o\varepsilon' \tan(\delta)$,[33] where ε_o is the permittivity of free space, ε' is the relative permittivity and $\tan(\delta)$ is the dielectric loss tangent. The variation of ac conductivity with frequency $\sigma(\omega)$ follows the Jonscher power law,[34] $\sigma(\omega) = \sigma_o + A\omega^n$, where σ_o is the dc conductivity obtained by extrapolating the conductivity to the lowest angular frequency, A is the pre-exponential factor and n represents the degree of interaction between the mobile ions and the surrounding ions in the lattice.[35] It is observed from Fig. 6(a–c) that the ac conductivity increases with frequency at different temperatures. Fig. 6(d) shows the variation of the logarithm of ac conductivity with the reciprocal of temperature at a frequency of 1 KHz. The ac conductivity (σ) of pristine and Fe (2 and 4 at%) doped $SrSnO_3$ nanoparticles at room temperature (310 K) is found to be 3.23×10^{-8}, 3.98×10^{-8} and 4.47×10^{-8} Ω^{-1} cm^{-1}, respectively. Evidently, the conductivity increases with doping concentration as the charge carriers get

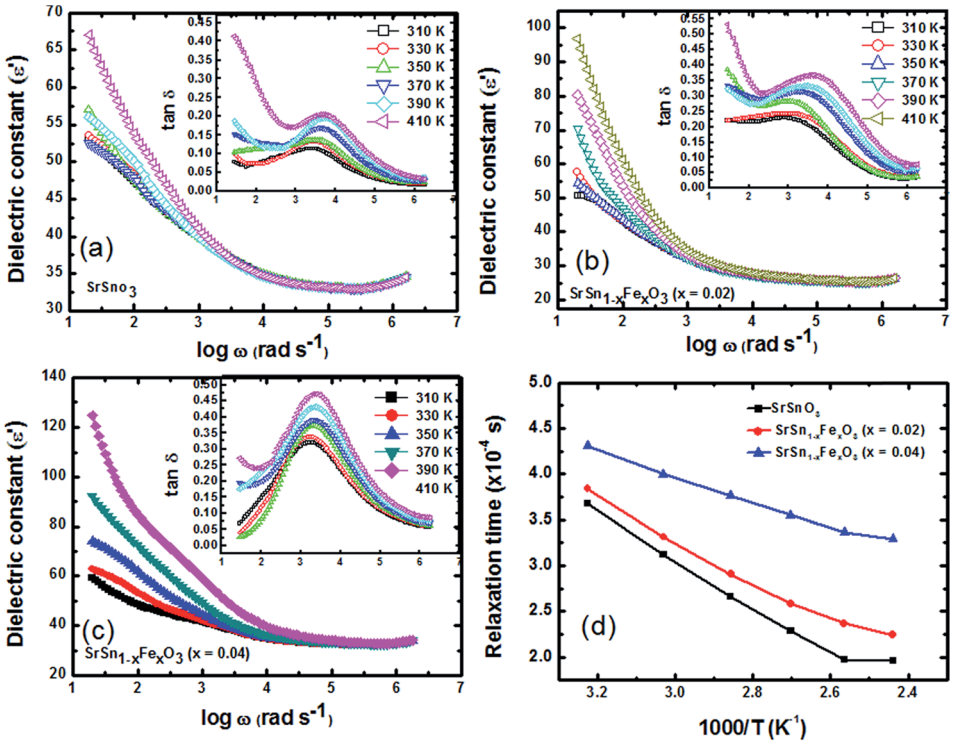

Fig. 5 (a–c) Frequency dependent dielectric constant (ε') and inset shows the variation of loss tangent of pristine and Fe (2 and 4 at%) doped $SrSnO_3$ nanoparticles at different temperatures, and (d) the variation of relaxation time with temperature and Fe content.

enhanced in the band region of $SrSnO_3$. The activation energy (E_a) of pristine and Fe (2 and 4 at%) doped $SrSnO_3$ was calculated using the Arrhenius relation. The activation energy was found to be 0.22, 0.34 and 0.42 eV for the pristine and Fe (2 and 4 at%) doped $SrSnO_3$ nanoparticles, respectively. The hopping frequency has been estimated by Jonscher power law

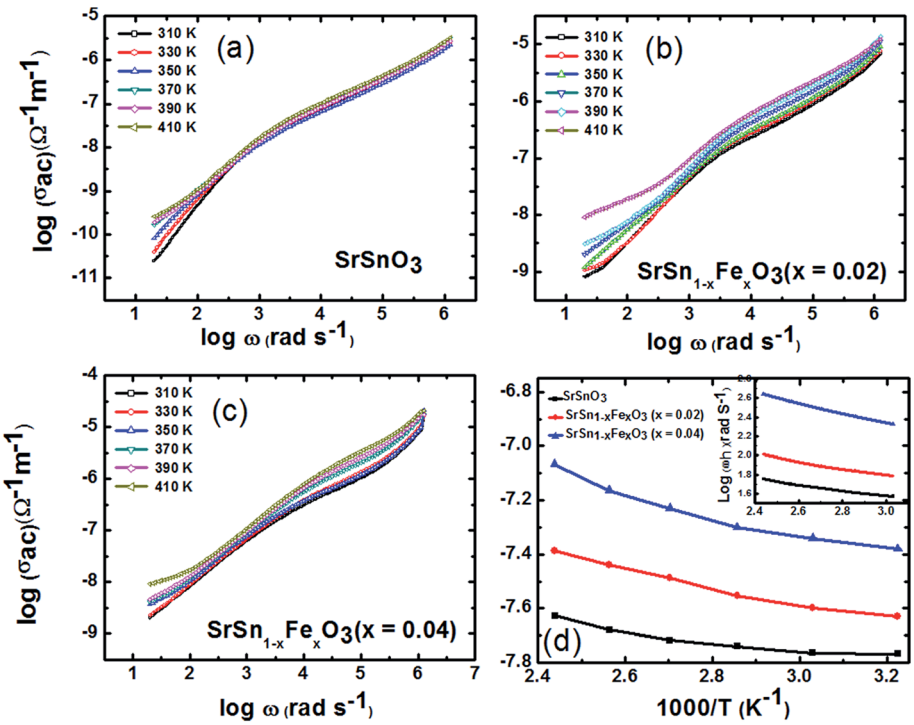

Fig. 6 (a–c) Frequency dependent ac conductivity and (d) shows the variation of ac conductivity and inset shows the variation of the hopping frequency of pristine and Fe (2 and 4 at%) doped $SrSnO_3$ nanoparticles at different temperatures.

proposed by Almond–West and given by expression $\sigma_{ac} = \sigma_{dc}[1 + (\omega/\omega_h)^s]$,[36,37] where ω_h is the hopping frequency of the charge carriers. Fig. 6(d) shows the variation of the logarithm of hopping frequency (ω_h) with a reciprocal of temperature. The temperature dependent hopping frequency (ω_h) is known to obey Arrhenius relation as, $\omega_h = \omega_o e^{(-E_w/KT)}$, where ω_o is the pre exponential factor, and E_w is the hopping activation energy. The hopping activation energy was found to be 0.25, 0.31 and 0.41 eV for pristine and Fe (2 and 4 at%) doped $SrSnO_3$ nanoparticles, respectively. The activation energy and hopping activation energy was found to be approximately same, which conveys that the mobility of charge carriers in the lattice may be due to the hopping mechanism.

4. Conclusions

The composition $SrSn_{1-x}Fe_xO_3$ has been synthesized successfully by a wet chemical route. X-ray diffraction patterns revealed the formation of orthorhombic phase $SrSnO_3$ nanoparticles. HRTEM images confirm the formation of nanoparticles having particle size around 20 nm. It has been observed that Fe substitution on Sn site has a considerable effect on the dielectric behavior of the material. The relative permittivity as a function of frequency at different temperatures was found to increase with temperature and Fe content. The relaxation time was found to decrease with temperature and increase with Fe content. The ac conductivity values and activation energies were found to increase with increase in the Fe content.

Acknowledgements

This study was supported by SERB, Government of India (SERB/F/1769/2013-2014).

References

1 W. F. Zhang, J. Tang and J. Ye, *Chem. Phys. Lett.*, 2006, **418**, 174–178.
2 S. Ouni, S. Nouri, H. Khemakhem and R. B. Hassen, *Mater. Res. Bull.*, 2014, **51**, 136–140.
3 Y. Li, H. Zhang, B. Guo and M. Wei, *Electrochim. Acta*, 2012, **70**, 313–317.
4 G. Prathiba, S. Venkatesh and N. H. Kumar, *Solid State Commun.*, 2010, **150**, 1436–1438.
5 Q. Z. Liu, H. F. Wang, F. Chen and W. J. Wu, *J. Appl. Phys.*, 2008, **103**, 093709.
6 G. Prathiba, S. Venkatesh, K. K. Bharathi and N. H. Kumar, *J. Appl. Phys.*, 2011, **109**, 07C320.
7 A. M. Azad, L. L. W. Shyam and M. A. Alim, *J. Mater. Sci.*, 1999, **34**, 1175–1187.
8 C. W. Lee, D. W. Kim, I. S. Cho, S. Park, S. S. Shin, A. W. Seo and K. S. Hong, *Int. J. Hydrogen Energy*, 2012, **37**, 10557–10563.
9 A. L. Goodwin, A. T. Redfern, M. T. Dove, D. A. Keen and M. G. Tucker, *Phys. Rev. B: Condens. Matter Mater. Phys.*, 2007, **76**, 174114.
10 A. Kumar, R. N. P. Choudary, B. P. Singh and A. K. Thakur, *Ceram. Int.*, 2006, **32**, 73–83.
11 A. M. Azad, T. Y. Pang and M. A. Alim, *Act. Passive Electron. Compon.*, 2003, **26**, 151–166.
12 J. Bohnemann, R. Libanori, M. L. Moreira and E. Longo, *Chem. Eng. J.*, 2009, **155**, 905–909.
13 D. K. Patel, B. Rajeswari, V. Sudarsan, R. K. Vatsa, R. M. Kadam and S. K. Kulshreshtha, *Dalton Trans.*, 2012, **41**, 12023.
14 S. Ouni, S. Nouri, J. Rohlicek and R. B. Hassen, *J. Solid State Chem.*, 2012, **192**, 132–138.
15 W. Zhang, J. Tang and J. Ye, *J. Mater. Res.*, 2007, **22**, 1859–1871.
16 C. Li, Y. Zhu, S. Fang, H. Wang, Y. Gui, L. Bi and R. Chen, *J. Phys. Chem. Solids*, 2011, **72**, 869–874.
17 X. Wang and S. Zhang, *Mater. Sci. Eng., B*, 2001, **86**, 29–33.
18 S. Soleimanpour and F. Kanjouri, *Phys. B*, 2014, **432**, 16–20.
19 X. Han, X. Li, X. Long, H. He and Y. Cao, *J. Mater. Chem.*, 2009, **19**, 6132–6136.
20 T. Endo, T. Masuda, H. Takizawa and J. Shimada, *J. Mater. Sci. Lett.*, 1992, **11**, 1330–1332.
21 S. Singh, P. Singh, O. Prakash and D. Kumar, *Adv. Appl. Ceram.*, 2007, **106**, 5.
22 O. Pakash, K. D. Mandal, C. C. Christopher and M. S. Sastry, *J. Mater. Sci. Lett.*, 1996, **31**, 4705–4708.
23 G. L. Lucena, A. S. Maina, A. G. Souza and I. M. G. Santos, *J. Therm. Anal. Calorim.*, 2014, **115**, 137–144.
24 M. Glerup, K. S. Knight and F. W. Polusen, *Mater. Res. Bull.*, 2005, **40**, 507–520.
25 E. Moreira, J. M. Henriques, D. L. Azevedo, E. W. S. Caetano, V. N. Freire and E. L. Albuquerque, *J. Solid State Chem.*, 2011, **184**, 921–928.
26 H. Cui, Y. Lui, W. Ren, M. Wang and Y. Zhao, *Nanotechnology*, 2013, **24**, 345602.
27 A. Kumar and J. Kumar, *Solid State Commun.*, 2008, **147**, 405–408.
28 H. Guo, R. Mao, D. Tian, W. Wang, D. Zhao, X. Yang and S. Wang, *J. Mater. Chem. A*, 2013, **1**, 3652.
29 M. Tarrida, H. Larguem and M. Mardon, *Phys. Chem. Miner.*, 2009, **36**, 403–413.
30 H. Gökce and S. Bahçeli, *Opt. Spectrosc.*, 2013, **115**(5), 632–644.
31 D. Chen and J. Ye, *Chem. Mater.*, 2007, **19**, 4585–4591.
32 S. Das, D. Y. Kim, C. M. Choi and Y. B. Hahn, *Mater. Res. Bull.*, 2013, **46**, 609–614.
33 C. Sevik and C. Bulutay, *Phys. Rev. B: Condens. Matter Mater. Phys.*, 2006, **74**, 193–201.
34 S. Kumar and K. B. R. Varma, *Curr. Appl. Phys.*, 2011, **11**, 203–210.
35 A. K. Jonscher, *Nature*, 1977, **267**, 673.
36 S. Kumar and K. B. R. Varma, *Solid State Commun.*, 2008, **146**, 137–142.
37 D. P. Almond and A. R. West, *Nature*, 1983, **306**, 455.